Materials & Design 226 (2023) 111631

Contents lists available at ScienceDirect

Materials & Design

journal homepage: www.elsevier.com/locate/matdes

Virtual heat treatment for γ-γ′ two-phase Ni-Al alloy on the materials Integration system, MInt

Toshio Osada [a,*], Toshiyuki Koyama [b], Dmitry S. Bulgarevich [a], Satoshi Minamoto [a], Makoto Osawa [a], Makoto Watanabe [a], Kyoko Kawagishi [a], Masahiko Demura [a]

[a] National Institute for Materials Science, Tsukuba, Japan
[b] Department of Materials Design Innovation Engineering, Nagoya University, Nagoya, Japan

HIGHLIGHTS

- A novel computational workflow implemented on the Materials Integration system (MInt) for virtual heat treatment for Ni-Al alloy was developed.
- The workflow implemented in MInt was constructed by integrating the PF simulation, image analysis, and mechanical property prediction modules.
- The workflow calculates the effects of aging process conditions, precipitates size, volume fraction, and Al concentration on 0.2 % proof stress.
- Virtual heat treatment on the system enables efficient design of optimal aging treatment conditions.

GRAPHICAL ABSTRACT

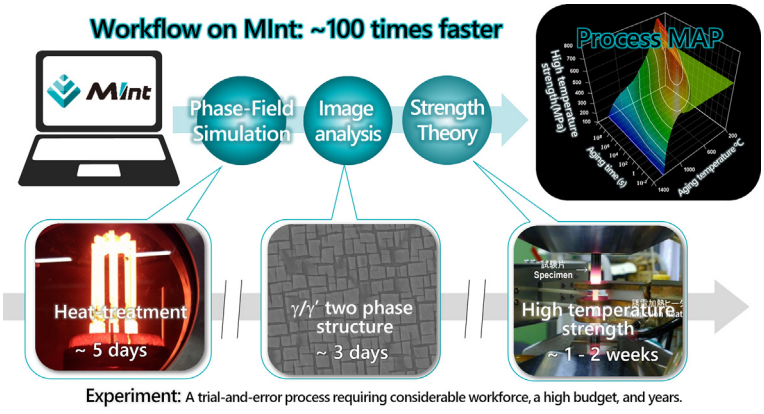

ARTICLE INFO

Article history:
Received 4 November 2022
Revised 9 January 2023
Accepted 13 January 2023
Available online 16 January 2023

Keywords:
Ni-Al alloy
γ-γ′ two-phase
Phase field simulation
Image analysis
Proof stress

ABSTRACT

Aiming to designing the aging heat treatment conditions to maximize the 0.2 % proof stress of γ-γ′ two-phase Ni-based superalloys, we develop the automated computational workflow for γ-γ′ two-phase Ni-Al binary alloy that serves at the system foundation. This consists of phase-field (PF) simulation, image analysis, and mechanical property prediction with the design of input and output data ports. The workflow is implemented on the Materials Integration system (MInt), which computationally links process, structure, property, and performance. Users may calculate any patterns in heat treatment scheduling for Ni-Al alloys, with various Al contents, by allowing MInt to conduct the workflow. First, MInt conducts multiple parallel runs of the PF simulation to generate statistically sound datasets. Subsequently, MInt extracts statistics of various microstructure/phase-geometrical/composition attributes by image analysis. Finally, it predicts the proof stress according to the reported superposition of multiple strengthening models. The established computational workflow provides an in-depth understanding of the effect of aging conditions on alloy strength, which is favorable for optimizing process.

1. Introduction

Ni-based superalloys with γ-γ′ two-phase structure are used as core parts of high-temperature turbine components in aircraft

* Corresponding author.
E-mail address: OSADA.Toshio@nims.go.jp (T. Osada).

https://doi.org/10.1016/j.matdes.2023.111631
0264-1275/

engines and land-based gas turbines because of their excellent high-temperature mechanical properties and oxidation resistance. In the latest Ni-based superalloys, the required performance for high-temperature strength properties is satisfied by multiple strengthening mechanisms (activated by more than ten alloying elements) [1] and a complex hierarchical microstructure [2,3]. In addition, their microstructural features are adjusted by casting, billeting, forging, and heat treatment at high temperatures, and the microstructure is fixed using final aging heat treatment. Optimizing the conditions in these multiple processes is typically a trial-and-error process requiring considerable workforce, a high budget, and years of development. Therefore, an accurate and systematic understanding of the process-structure–property-performance (PSPP) linkage is vital for component design, particularly in aircraft engine components requiring a high degree of reliability.

Numerous reports have presented the efforts carried out to develop PSPP prediction systems. Pioneering works include those of iron and steel materials reported by Bhadeshia et al. [4] and those of Ni-based superalloys for high-temperature applications reported by Harada et al. [1,5] and Reed. [2,6] In particular, the TMS alloy designed with the program [1] developed by Harada et al. has been used as the latest aircraft engine turbine component; this demonstrates that a computational prediction system can help design new alloys. More recently, several computational materials design techniques, in integrated computational materials engineering, have been proposed to support the improvement of component performance by predicting the distribution of mechanical properties and microstructural features in engine components. For example, the prediction system proposed by Olson et al. [7] in Materials Genome Initiative in the U.S. and the method proposed by C. Rae et al. [8] in the U.K. indicate the possibility of performance prediction from process and microstructure information. Furthermore, the commercial software, JMatPro, [9,10] can predict physical and mechanical properties from the microstructure of various alloys with a certain degree of accuracy. As a result, it is widely used in manufacturing, particularly in casting and forging companies.

Materials Integration (MI) [11–15] is a concept used to accelerate the research and development of materials by computationally linking the PSPP using any prediction model, such as numerical simulation, theoretical or empirical theory, and data-driven regression. Based on this concept, a versatile system for materials design [16] was investigated by our group. This system was named MInt, denoted by Materials Integration with Network Technology [11]. Computational materials design tools, particularly the efficient PSPP prediction system, have attracted considerable attention in recent years in developing advanced components. In addition to high-temperature strength properties, predicting multiple other properties, such as fatigue and creep properties [14], by optimizing the process conditions and microstructural features is important.

This study aims to demonstrate the usefulness of MI for developing the γ-γ' two-phase Ni-Al binary alloy. We developed a computational workflow that can predict the high-temperature strength from the microstructure evolution via the heat treatment process. The workflow consisted of three modules, including the phase-field (PF) simulation module, image analysis module, and mechanical property prediction module. These modules were implemented and consistently connected to form a workflow in MInt, allowing automatic computation of 0.2 % proof stress at any high temperature for any heat treatment scheduling. The validity and basic performance of the constructed workflow in Ni-Al binary alloys were examined, which is a step prior to applying the workflow for practical superalloys. Based on the analysis of the computed virtual data set for several isothermal aging conditions, a process map with a wide range of process conditions was constructed, demonstrating the practicality and usefulness of the workflow to effectively design heat treatment scheduling.

2. Workflow to high-temperature strength from heat treatment scheduling

2.1. Workflow design

In this study, we focused on the aging heat treatment that determines the final performance in Ni-Al alloys with a γ-γ' two-phase structure and developed a workflow to predict 0.2 % proof stress at high temperatures from the heat treatment scheduling. Fig. 1 presents a screenshot of the constructed workflow taken from the graphical user interface (GUI) for the workflow design in MInt.

The initial field generation module was prepared to generate an initial field for the PF simulation. Each of the modules receives necessary information through input ports and outputs the computed results through output ports. In Fig. 1, input ports, modules, and output ports are shown in blue, yellow, and gray, respectively. First, the alloy compositions and aging conditions were fed from the input ports to the PF simulation module, which uses the initial field provided by the initial field generation module. Next, the computed microstructure output from the PF simulation module was fed through the input port to the image analysis module. The image analysis module extracts the statistics of the composition and microstructure, such as the mean Al concentrations in the γ and γ' phases, the average size, and mole fraction of the γ' phase. The output and input ports are concealed in the line between the two modules (Fig. 1). To obtain reliable statistics, duplicate computations were conducted in parallel, starting from different initial fields. Here, 30 individual computations were conducted, the number of which can be specified through the input ports of the initial field generation module. Finally, the mechanical property prediction module receives the composition and microstructure information from the image analysis module and outputs 0.2 % proof stress at an arbitrary test temperature, which can also be specified through the input port of this module. As mentioned in Section 2.4, 0.2 % proof stress was computed according to the theoretical and empirical equations [3,9,17,18] based on the following inputs: test conditions (strength test temperature), composition and microstructure information (alloy composition, γ composition, size, and volume fraction of γ' precipitations), and material properties (Poisson's ratio, Burgers vector, Taylor factor, anti-phase boundary energy, and melting point).

Another feature of this workflow is its flexibility to adjust to the purpose of the user. Making changes in the phase diagram, properties used in the PF simulation module, and physical properties used in the mechanical property prediction module can be carried out with relative ease. This demonstrates that the workflow can widen the prediction applicable range from the binary system to a more complicated one for practical Ni-based superalloys.

The obtained composition-process-structure–property data sets are systematically stored in MInt for analyzing inverse problems, where one may optimizes the composition and/or process from the desired property. This study focuses on the forward problem analysis; the inverse analysis using this workflow will be reported in the future.

2.2. Phase-field simulation module

The γ' precipitation and the microstructure developments in Ni-based alloys were simulated based on the PF model [19–24]. The PF model proposed by Vaithyanathan and Chen [23] was employed as

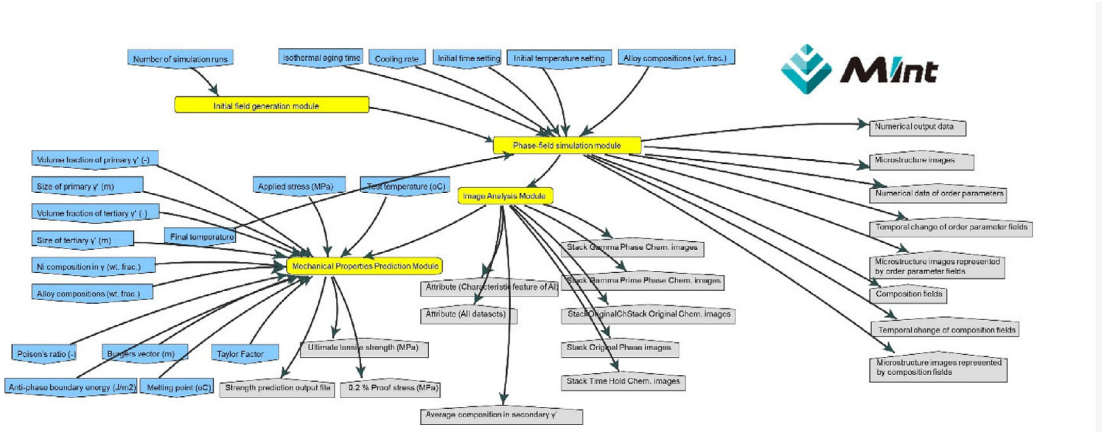

Fig. 1. Screenshot of the constructed workflow design for high-temperature mechanical properties prediction taken from graphical user interface in Materials Integration by network technology (MInt) system.

a base model in this study, and the chemical free energy part was slightly modified to introduce the Kim–Kim–Suzuki (KKS) model [25], as mentioned below. In this section, the outline of the simulation method is explained using the phase decomposition in Ni-Al binary alloy system as an example.

The order parameters, which describe the microstructure changes, are the Al solute composition field $c(\boldsymbol{r},t)$ and the long-range order parameter fields $s_i(\boldsymbol{r},t),(i=1,2,3)$ represent the $L1_2$ ordering of γ' phase, where the subscript i is utilized to distinguish the four variants in the $L1_2$ ordered structure [23]. These order parameters are the functions of local position $\boldsymbol{r}=(x,y,z)$ and time t. The governing equations to calculate the microstructure changes are given as equations (1) and (2):

$$\frac{\partial c(\boldsymbol{r},t)}{\partial t}=M_c\nabla^2\left(\frac{\delta G_{\rm sys}}{\delta c(\boldsymbol{r},t)}\right) \tag{1}$$

$$\frac{\partial s_i(\boldsymbol{r},t)}{\partial t}=-M_s\frac{\delta G_{\rm sys}}{\delta s_i(\boldsymbol{r},t)},(i=1,2,3), \tag{2}$$

where M_c and M_s are the mobility of atom diffusion and the relaxation coefficient of the long-range order parameter field, respectively. Moreover, the total free energy of the microstructure $G_{\rm sys}$ is defined by $G_{\rm sys}\equiv G_{\rm c}+E_{\rm grad}+E_{\rm str}$ in terms of the chemical free energy $G_{\rm c}$, gradient energy $E_{\rm gard}$, and elastic strain energy $E_{\rm str}$. These energies are evaluated using the following equations.

$$G_{\rm c}=\int_{\boldsymbol{r}}\{G_{\rm c}^{\gamma}(f_m,T)\{1-h(\phi)\}+G_{\rm c}^{\gamma\prime}(f_p,T)h(\phi)+W_{12}g(\phi)\}d\boldsymbol{r}, \tag{3}$$

$$E_{\rm grad}=\int_{\boldsymbol{r}}\{\frac{1}{2}\kappa_s(|\nabla s_1|^2+|\nabla s_2|^2+|\nabla s_3|^2)\}d\boldsymbol{r}, \tag{4}$$

$$\begin{aligned}E_{\rm str}&=\tfrac{1}{2}\int_{\boldsymbol{r}}C_{ijkl}\{\varepsilon_{ij}^{\rm c}(\boldsymbol{r},t)-\varepsilon_{ij}^{0}(\boldsymbol{r},t)\}\{\varepsilon_{kl}^{\rm c}(\boldsymbol{r},t)-\varepsilon_{kl}^{0}(\boldsymbol{r},t)\}d\boldsymbol{r}\\&=\tfrac{1}{2}\int_{\boldsymbol{k}}B(\boldsymbol{n})Q(\boldsymbol{k},t)Q(-\boldsymbol{k},t)\tfrac{d\boldsymbol{k}}{(2\pi)^3},\end{aligned} \tag{5}$$

$$G_{\rm c}^{\gamma}(f)=\frac{1}{2}W_1f^2,\quad G_{\rm c}^{\gamma\prime}(f)=\frac{1}{2}W_2(1-f)^2 \tag{6}$$

$$f(\boldsymbol{r},t)\equiv\frac{c(\boldsymbol{r},t)-c_m^0(T)}{c_p^0(T)-c_m^0(T)} \tag{7}$$

$$h(\phi)\equiv\phi^3(10-15\phi+6\phi^2),\ \ g(\phi)\equiv\phi^2(1-\phi)^2 \tag{8}$$

$$\phi^3(\boldsymbol{r},t)\equiv s_1(\boldsymbol{r},t)s_2(\boldsymbol{r},t)s_3(\boldsymbol{r},t) \tag{9}$$

$$\varepsilon_{ij}^{0}(\boldsymbol{r},t)\equiv\delta_{ij}\eta_0\{c(\boldsymbol{r},t)-c_0\}=\delta_{ij}\frac{\varepsilon_0}{c_p^0(T)-c_m^0(T)}\{c(\boldsymbol{r},t)-c_0\}, \tag{10}$$

$$\begin{aligned}B(\boldsymbol{n})&=(C_{11}+2C_{12})\varepsilon_0^2\\&\times\left[3-\frac{(C_{11}+2C_{12})\left[1+2\xi(n_1^2n_2^2+n_2^2n_3^2+n_3^2n_1^2)+3\xi^2n_1^2n_2^2n_3^2\right]}{\left[C_{11}+\xi(C_{11}+C_{12})(n_1^2n_2^2+n_2^2n_3^2+n_3^2n_1^2)+\xi^2(C_{11}+2C_{12}+C_{44})n_1^2n_2^2n_3^2\right]}\right],\end{aligned} \tag{11}$$

where $f(\boldsymbol{r},t)$ is a local volume fraction field of the γ' phase; $c_m^0(T)$ and $c_p^0(T)$ are the equilibrium compositions of the γ and γ' phases, respectively, given as functions of temperature T; and $G_{\rm c}^{\gamma}(f,T)$ and $G_{\rm c}^{\gamma\prime}(f,T)$ are the Gibbs energies of the γ and γ' phases, respectively. Herein, the Gibbs energy functions were approximated to quadratic form with respect to $f(\boldsymbol{r},t)$, where the coefficients W_1, W_2, and W_{12} were determined using the Gibbs energy curve calculated from the thermodynamic Gibbs energy parameters in the calculation of the phase diagram (CALPHAD) method [26]. The interpolation function $h(\phi)$ and energy barrier function $g(\phi)$ are the standard functions, which are typically employed in the multi-phase field method [21]. The phase-field order parameter $\phi(\boldsymbol{r},t)$, which calculates the probability of finding a γ' phase at position $\boldsymbol{r}$ and time t in the microstructure, is defined as a function of $s_i(\boldsymbol{r},t)$. Note that the above definition $\phi^3\equiv s_1s_2s_3$ provides the four variants of the $L1_2$ ordered structure because the condition $\phi^3\equiv s_1s_2s_3=1$ corresponds to four cases [23]:

$$\begin{aligned}&(s_1,s_2,s_3)=(1,1,1)\\&(s_1,s_2,s_3)=(1,-1,-1)\\&(s_1,s_2,s_3)=(-1,1,-1)\\&(s_1,s_2,s_3)=(-1,-1,1)\end{aligned} \tag{12}$$

In addition, any two $s_i,(i=1,2,3)$ are guaranteed to be zero at the antiphase boundary. Here, κ_s is the gradient energy coefficient with respect to the long-range order parameter field $s_i(\boldsymbol{r},t)$. The composition gradient energy term was not considered because the Kim–Kim–Suzuki (KKS) model [25] was used to calculate the local chemical potential. In the evaluation of elastic strain energy, the phase-field micro-elasticity theory was used [22–24], where $\varepsilon_{ij}^{\rm c}$ and ε_{ij}^{0} are the total strain and the eigen strain, respectively. Herein, $Q(\boldsymbol{k},t)$ is the Fourier transform of $c(\boldsymbol{r},t)-c_0$, where c_0, $\boldsymbol{k}$, and $\boldsymbol{n}$ are the average solute composition, Fourier vector, and the unit vector along the $\boldsymbol{k}$ direction, respectively. C_{ijkl} is the elastic stiffness which was assumed to be constant in this calculation, that is,

the elastically homogeneous case was considered for simplicity. According to the Vegard's law [22], the eigen strain ε_{ij}^0 is proportional to the local composition; η_0 and δ_{ij} are the lattice mismatch; and the Kronecker delta: $\delta_{ij} = 1$ for $i = j$ and $\delta_{ij} = 0$ for $i \neq j$. Here, η_0 is defined as $\eta_0 \equiv \varepsilon_0/\{c_p^0(T) - c_m^0(T)\}$, and ε_0 is the eigen strain between the γ matrix and γ′ precipitate, each of which has the equilibrium composition [27].

The temporal evolution of the microstructure change was simulated based on the conventional deference method, and dimensionless formalism was applied. Following the assumption of the dimensionless mobility terms, $M_c = 1$ and $M_s = 1$, the diffusion constant $D(T)$ of the solute Al atoms [28] was utilized to convert the dimensionless aging time to real-time. The details of the numerical calculation are available in reported works [19,24], and the materials parameter values utilized in this study are summarized in Table 1. Note that we assumed the gradient energy coefficient to be constant over the calculation temperature range, since the influence of the temperature dependence part in gradient energy coefficient on the γ′ evolution is neglectable. The initial microstructure was prepared by using the initial field generation module (Fig. 1), which is the short-term phase-field simulation from a supersaturated solid solution with a small composition fluctuation, generated by the random number computationally. The output simulation results are the order parameter fields, $c(\boldsymbol{r}, t)$ and $s_i(\boldsymbol{r}, t), (i = 1, 2, 3)$, and the field data was saved in the visualization toolkit (VTK) file format [29].

In the PF simulation module, because the basic unit of the heat treatment was set as isothermal aging followed by continuous cooling (or heating), any heat treatment process can be represented by combining units. To improve the simulation speed, the temperature dependence of the equilibrium compositions, in the γ′ and γ′ phases, was calculated in advance and approximated by using the expansion formula (Table 1). As isothermal aging is considered in the current work, the detailed explanation about handling the complex heat treatment was omitted in this paper.

2.3. Image analysis module

The outputted VTK files from the PF simulation module were used for extracting microstructure geometrical and phase composition attributes with the image analysis module. The module converts the VTK datasets with $s_i(\boldsymbol{r}, t)$ and Al at. % to the corresponding image stacks. The VTK data were collected and analyzed at the end of the heat treatment schedule. If needed, the time domain data could be pulled from PF simulations. $s_i(\boldsymbol{r}, t)$, the γ′-phase volume fraction f_V, as well as various geometrical attributes for each γ′-object (including area, perimeter, Feret diameters, circularity, solidity, aspect ratio, and their corresponding statistical means) were extracted from the image stack. Consequently, the user can judge based on their standard deviations and, if necessary, increase the number of simulated areas in repeated PF simulations. From the image stack with Al at. % distribution, the mean Al concentrations of c_m^{Al} in γ, c_p^{Al} in γ′, and c^{Al} in all phases were extracted. Subsequently, they were passed, together with the mean diameter of a circle with an equal projection area for γ′-objects ($d = 2\sqrt{\overline{Area}/\pi}$), to the mechanical properties prediction module. Here, we should note that area fraction f_A obtained from 2D PF simulations is equal to volume fraction f_V, since 2D PF simulation result was calculated by using the phase diagram information ($c_m^0(T)$ and $c_p^0(T)$) as shown in Table 1.

2.4. Mechanical properties prediction module

The mechanical property prediction module is based on reported theoretical or empirical models for Ni-based superalloys with γ-γ′ two-phase structure [3,8,17,18]. The outline of the calculation method for 0.2 % tensile proof stress, $\sigma_{0.2}$, as well as the solid-solution and precipitation strengthening in the Ni-Al binary single crystal alloy system is explained as follows.

Herein, a strengthening model described by the superposition of all the strengthening factors [17] was utilized. Additionally, solid solution $\Delta\sigma_{ss}$ and precipitation $\Delta\sigma_{\gamma'}$ strengthening were considered as follows.

$$\sigma_{0.2} = \sigma_{Ni} + \Delta\sigma_{ss} + \Delta\sigma_{\gamma'} = M(\tau_{Ni} + \Delta\tau_{ss} + \Delta\tau_{\gamma'}), \tag{13}$$

where τ_{Ni} is the strength of pure nickel single crystal and M is the reciprocal number of the Schmid factor of alloy, M = 2.449 (for polycrystalline FCC alloy, M is the Taylor factor; M = 3.1). In this study, the reported value for the strength of pure Ni was used [2]. The details of the superposition of each strengthening model used can be found in the references [3,17,18].

The conventional theory for solid-solution strengthening (SSS) in the alloy has been proposed by Fleisher [30] and Labusch [31]. A model of SSS for multi-component [32], such as superalloy [33] and high-entropy alloy [34], has been proposed. The critical threshold stress of SSS for binary alloy, known as Labusch limit, is found to be [31,35,36]:

$$\Delta\tau_{ss} = \left(\frac{F_m^4 w_e}{4Gb^9}\right)^{\frac{1}{3}} c^{\frac{2}{3}}, \tag{14}$$

where b is the magnitude of Burgers vector of the edge dislocation in the γ matrix; G is the shear modulus; c is the atomic concentra-

Table 1
Numerical values used for the phase-field simulation.

Coefficients in chemical free energy* ($J \cdot mol^{-1}$)	$W_1 = 2.236 \times 10^3$, $W_2 = 3.106 \times 10^3$, $W_{12} = 1.379 \times 10^3$
Gradient energy coefficient [28], κ_s ($J \cdot m^2 \cdot mol^{-1}$)	1.826×10^{-15}
Elastic constants [29] (GPa)	$C_{11} = 250.8$, $C_{12} = 150.0$, $C_{44} = 123.5$
Eigen strain between γ matrix and γ′ precipitate [27], ε_0	0.006
Diffusion coefficient of Al atoms [29], $D(T)$ ($m^2 \cdot s^{-1}$)	$D(T) = 5.0 \times 10^{-4} \exp\left(-\frac{2.60 \times 10^5}{RT}\right)$, R: Gas constant $/J \cdot K^{-1} \cdot mol^{-1}$, T: Temperature /K
Equilibrium compositions (atomic fraction of Al) of γ and γ′ phases*: $c_m^0(T) = 1.077535 \times 10^{-2} + 1.554659 \times 10^{-4}T - 7.521288 \times 10^{-8}T^2 + 3.366849 \times 10^{-11}T^3$, $c_p^0(T) = 2.118598 \times 10^{-1} + 1.548849 \times 10^{-4}T - 1.836197 \times 10^{-7}T^2 + 4.357137 \times 10^{-11}T^3 + 1.052733 \times 10^{-14}T^4$	

* Numerically approximated by using the available Gibbs energy [25].

tion of solute atom; w_e ($2b$ to $3b$) [37] is the range of interaction between obstacles and dislocation; and F_m is the maximum interaction force between a dislocation and an obstacle. F_m is approximately equal to $Gb^2 sin\theta_c$, where θ_c is a critical angle of dislocation interacted with the obstacle. Thus, $\Delta\tau_{SS}$ strongly depends on the shear modulus G of the alloy system. For the Ni-Al binary system in this study, the value of $\left(\frac{F_m^4 w_e}{4Gb^9}\right)^{\frac{1}{3}}$ = 5.745 (MPa/atm$^{2/3}$) was used from the experimental values [36].

Precipitation strengthening $\Delta\tau_{\gamma'}$ can be described as follows.

$$\Delta\tau_{\gamma'} = \Delta\tau_{\gamma'}^{ROM} + \Delta\tau_{\gamma'}^{P}, \tag{15}$$

where $\Delta\tau_{\gamma'}^{ROM}$ and $\Delta\tau_{\gamma'}^{P}$ are contributions by the rule of mixture (ROM) and precipitation/dislocation interaction, respectively [19]. Based on the typical mixture theory, the strength increments caused by the embedded secondary precipitates within the matrix can be described by the isoworks criteria [18,38]. The value lies between the Voigt and Reuss models described by isostress criteria, which show the upper and lower bounds, respectively, as follows.

$$\Delta\tau_{\gamma'}^{Voigt} = (\tau_{\gamma'} - \tau_{Ni} - \Delta\tau_{ss})f_V,$$

and

$$\Delta\tau_{\gamma'}^{Reuss} = \left\{\frac{\tau_{\gamma'}}{\tau_{\gamma'}(1-f_V) + (\tau_{Ni} + \Delta\tau_{ss})f_V} - 1\right\}(\tau_{Ni} + \Delta\tau_{ss}),$$

where $\tau_{\gamma'}$ is the critical resolved shear stress (CRSS) of γ' single phase. In this study, we assumed that the strength increments caused by ROM could be estimated as the average of the upper and lower bounds in order to simplify the discussion. Thus, the rule of a mixture can be simply described using the following equation:

$$\Delta\tau_{\gamma'}^{ROM} = \left(\Delta\tau_{\gamma'}^{Voigt} + \Delta\tau_{\gamma'}^{Reuss}\right)/2 \tag{17}$$

Meanwhile, the CRSS of Ni_3Al suggests an inverse temperature dependence because the Keare-Wilsdorf (KW) locking controls the plastic deformation. In this study, we used an average CRSS on the (111)[−101] slip system in stoichiometric Ni_3Al (Ni-25 at. % Al) that was reported in reference [39].

As illustrated in Fig. 2, the precipitation strengthening $\Delta\tau_{\gamma'}^{P}$ is categorized primarily into three models, namely the weakly coupled pair-dislocation shear model $\Delta\tau_w^P$ (Fig. 2a), strongly coupled pair-dislocation shear model $\Delta\tau_s^P$(Fig. 2b), and Orowan bypassing model $\Delta\tau_{or}^P$ (Fig. 2c). The favor precipitation model in the system is selected depending on the volume fraction and size of γ'. Numerous researchers have attempted to model the strength increment by the precipitation/dislocation interaction. In this study, the proposed precipitation models [8,18] were used, and the one exhibiting the minimum value was selected as the favor model:

$$\Delta\tau_{\gamma'}^{P} = Min[\Delta\tau_{w,s}^{P}, \Delta\tau_{or}^{P}]$$

$$\Delta\tau_{w,s}^{P} = \begin{cases} \frac{2\gamma_{APB}}{b}\frac{r}{L}\left\{\frac{(2\gamma_{APB}r)^{\frac{1}{2}}}{(Gb^2)^{\frac{1}{2}}+(2\gamma_{APB}r)^{\frac{1}{2}}}\right\}, & if\ r < x_m (Weakly) \\ \frac{2\gamma_{APB}}{b}\frac{1}{L}\left\{\frac{(2\gamma_{APB}r)^{\frac{1}{2}}}{(Gb^2)^{\frac{1}{2}}+(2\gamma_{APB}r)^{\frac{1}{2}}}\right\}\left\{r^2 - \left(r - \frac{2}{\gamma_{APB}}\left(\frac{Gb^2}{2\pi}\right)\right)^2\right\}^{\frac{1}{2}}, & if\ r \geq x_m (Strongly) \end{cases}$$

$$\Delta\tau_{or}^{P} = \frac{3Gb}{2(L-2r)} \quad (Orowan\ bypassing) \tag{18}$$

where γ_{APB} is the anti-phase boundary (APB) energy of γ'; x_m is the critical distance between leading and trailing dislocations (as illustrated in Fig. 2b) regarding to the transition size defined as: $x_m = \frac{2}{\gamma_{APB}}\left(\frac{Gb^2}{2\pi}\right)$; and L is the mean particle spacing, defined as:

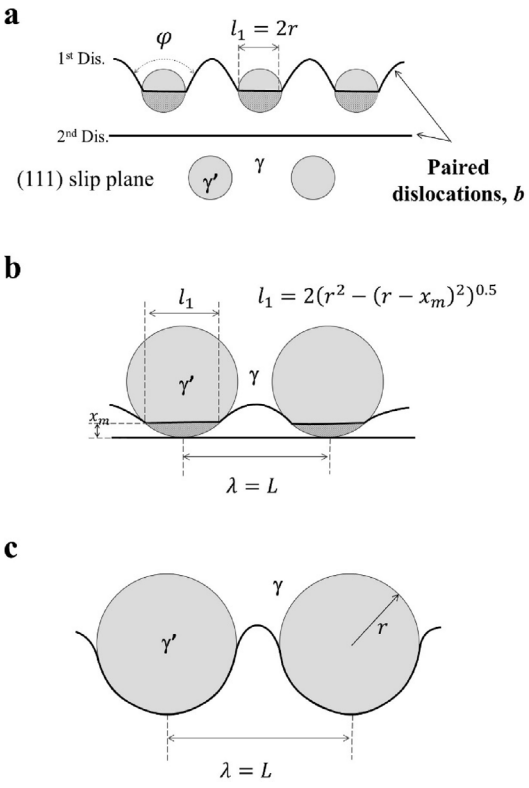

Fig. 2. Schematic of precipitation/dislocation interaction models: (a) weakly-coupled dislocations shear model, (b) strongly-coupled dislocations shear model, (c) Orowan bypassing model.

$$L = \left(\frac{2\pi}{3f_v}\right)^{\frac{1}{2}}\frac{d}{2} \tag{19}$$

By substituting equations (14)–(19) into equation (13), the 0.2 % proof stress can be estimated. In this study, high temperature 0.2 % proof stress was predicted by only considering the temperature dependence of shear modulus G and assuming b and θ_c to be constant at elevated temperatures. Moreover, γ_{APB} was assumed as a temperature-independent fitting parameter. Thus, γ_{APB} = 0.10 J/m^2 was used at all temperatures in this study. The reported experimental value of the APB energy of Ni_3Al (γ_{APB}) was approximately 0.17 J/m^2 for stoichiometric Ni_3Al (c_p^{Al} = 0.25) [40]. The value of γ_{APB} tends to decrease as the Al concentration decreases [41]. Therefore, in this study, γ_{APB} was selected to be slightly lower than the reported value. In addition, incorporating the APB prediction into the mechanical property prediction module could increase the accuracy of prediction [42]; illustrates the importance of the APB energy prediction and the future perspective.

3. Experimental conditions

3.1. Virtual experimental conditions

The Ni-Al binary alloy phase diagrams including to $c_m^0(T)$ and $c_p^0(T)$ used in the calculations are shown in Fig. 3**a**. As shown this figure, PF simulation module can be applicable the Al composition below 0.25. Further, the module can be applicable the temperature below the solidus line or eutectic temperature also shown in Fig. 3**a**. Ni-19.11 at. % Al was used in this study. Here we note that all the temperature and Al composition ranges described in this study are within the stable formation ranges of γ-γ′ two-phase systems in the binary Al-Ni system. The two-dimensional (2D) calcu-

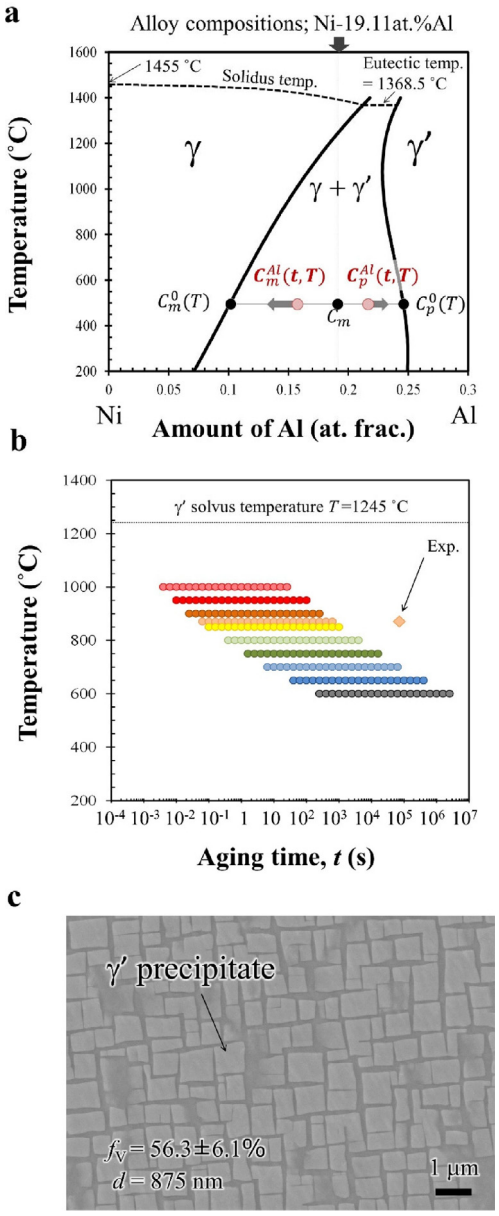

Fig. 3. (a) Phase-diagram of Ni-Al binary alloy used for phase-field calculation. (b) Input test conditions for aging heat treatment. (c) SEM image of microstructure of Ni-19.11 at. % Al aged at 870 °C for 20 h [44].

lation area of PF was set to 2 μm × 2 μm, and N = 30 calculations were performed for each aging heat treatment condition, changing the initial microstructure. The image analysis module was applied to the individual microstructure, and the average of the parameters obtained from the module was adopted as the output results. The parameters used in this process are listed in Table 1. The initial microstructure was set using the initial field generation module. To represent the rapidly cooled and supersaturated microstructure, the initial state was defined as the microstructure isothermally heat-treated at 1000 °C for 32 s. The characteristics of the obtained initial microstructures are summarized in Table 2. For these initial fields, as shown in Fig. 3**b**, calculations were performed using the PF simulation module (see Section 2.1) under 210 isothermal aging heat treatment conditions in the temperature range of 600–1000 °C and aging time ranging from 3.98107×10^{-3} to 3.98107×10^{5} s. Here, as the calculation area of the PF model used was 2 μm × 2 μm, the aging time was adjusted such that the precipitate size would be approximately 200 nm, corresponding to 1/10 of the model size under each temperature condition in consideration of calculation accuracy. For example, the maximum aging time was set to be approximately 10.5 min at 870 °C. Note that the time is shorter than the experimental conditions (870 °C/20 h) [43], as mentioned in the later section (Fig. 5a).

Using the image analysis module (see Section 2.2), the precipitate size d, volume fraction f_V, Al concentration c_m^{Al} in γ, and Al concentration c_p^{Al} in γ′ (which are important for the discussion on microstructure and property variations in Ni-Al binary alloys) were outputted for subsequent property prediction and discussion.

3.2. Physical experimental conditions

To confirm the accuracy of strength prediction, single-crystal model alloys [18] capable of evaluating precipitation strength and SSS were fabricated. The aging and high-temperature mechanical properties of these alloys were evaluated. The model alloy was Ni-19.11 at. % Al (9.8 wt%) with γ′ precipitation equivalent to that of a general Ni-based single crystal superalloy for blade applications, which was cast using a directional solidification furnace. Casted samples were subject to fast cooling (approximately 300 °C/min) with Ar gas after homogenization heat treatment at 1300 °C/5h to sufficiently homogenize microsegregation. The homogenized samples were subject to isothermal aging heat treatment at 870 °C for 20 h [43]. Moreover, γ single-phase single crystal model alloy, Ni-10.27 at. % Al (5.0 wt% Al), was prepared to evaluate the SSS. Here, the amount of Al in this alloy was designed to be less than 14.05 at. %, which is the equilibrium γ composition of Ni-19.11 at. % Al at 870 °C to suppress the fine cooling γ′ precipitations after the homogenization heat treatment.

The aged sample was machined into cylindrical specimens of 9 mm × 15 mm (Φ × L) and subject to compression tests at temperatures ranging from room temperature to 1100 °C. The strain rate for the compression test was 10^{-5} s^{-1}. The precipitated microstructure of the aged specimen (870 °C/20 h) was observed using field emission-scanning electron microscopy (FE-SEM; ZEISS, Gemini SEM 300). As shown in Fig. 3c, the γ′ precipitates were cuboidal in shape, with a volume fraction of 56.3 ± 6.1 % and precipitate size of 875 nm [44]. Here, γ′ area fraction f_A analyzed from the SEM images was 68.2 ± 4.7 %. However, in case of cuboidal precipitates, f_A is not equal to f_V. Thus, we calculated f_V from f_A by using the relation $f_V = f_A^{3/2}$, assuming that the precipitates shape is perfect cube shape as reported in [44].

Table 2
Initial microstructural features in phase-field simulation of Ni-19.11 at. % Al.

Alloy composition	Precipitate size d_o	Al concentration in γ′, c_p^{Al}	Al concentration in γ c_m^{Al}	Volume fraction of γ′, f_V^o
	nm	at. frac.	at. frac.	–
Ni-19.11Al	20.15	0.2200	0.1727	0.3916

4. Results

4.1. Microstructural evolutions

Al concentration contour plots (Fig. 4) show the time evolution of the microstructure at three temperatures (1000, 870, and 600 °C) obtained by the PF simulation module. The coarsening process of the γ′ phase was present at all temperatures. For the short aging time, the influence of the initial field and the small size of the γ′ phase resulted in the formation of irregularly shaped precipitates with a random Al concentration field. Subsequently, with increasing time, the γ′ precipitates changed to a cuboidal shape like the experimental microstructure in Fig. 3c. This is because the lattice mismatch $\eta_0 \equiv \varepsilon_0/\{c_p^0(T) - c_m^0(T)\}$ used in this study has a relatively large positive value [27]. Thus, we concluded that the simulation results were in good agreement with the experimental data of actual Ni-Al alloys [27]. Furthermore, for long term aging, a series of cuboidal γ′ shapes were observed in the ⟨100⟩ direction (top, bottom, left, and right directions in the figure). This was because of the influence of elastic interactions between adjacent γ′ precipitates [45] and the replacement of the anti-phase boundary (APB) of the γ′ phase by a thin γ phase [22], which demonstrated that the PF module reproduces these effects with good accuracy.

Fig. 5a – 5d show the aging temperature and time dependence of precipitate size d, volume fraction f_V, Al concentration c_m^{Al} in γ, and Al concentration c_p^{Al} in γ′, respectively. The data of the lines in Fig. 5 was estimated from equations (23) and (28), (29), (30), which are discussed in Section 5.2 and obtained via the image analysis module.

As shown in Fig. 5a, the precipitate size d increased with increasing aging temperature and aging time. On the log–log plot, all the results for long-term aging were linear, confirming that Ostwald ripening was exhibited according to the model presented in Section 3.2. The experimental results were located on the fitting line shown at 870 °C (which are discussed in Section 5.2); this implied that the model and the diffusion coefficient values of Al used in the calculations are highly valid.

By contrast, the volume fraction rapidly increased with increasing time in the early aging stage, reaching a value close to the equilibrium volume fraction at each temperature in the late aging stage. The equilibrium volume fraction at 870 °C was f_V^{eq} = 0.553, which is in good agreement with the experimental value. Therefore, the selected equilibrium phase diagram for the Ni-Al binary system [25] was considered a suitable candidate.

Note that the important feature of computer experiments using the PF method is the ability to easily output time dependence on Al concentration c_m^{Al} and c_p^{Al} in the γ and γ′ phases, respectively (Fig. 5c and 5d). Three-dimensional atom probe field ion microscopy (3DAP) is a common method for measuring elemental concentrations in nm-order sized precipitates and matrix. However, research on changes in element concentrations over time during aging is limited because an enormous amount of time and labor is required to analyze elemental concentrations under 210 heat treatment conditions similar to the situation in this study.

As shown in Fig. 5c, the Al concentration in the matrix phase significantly decreased with time in the early aging stage from the initial concentration of c_m^{Al} = 0.1727 and slowly decreased toward the equilibrium Al concentration at each temperature in the late aging stage. Furthermore, the Al concentration in the γ′ phase rapidly increased with time in the early aging stage and slowly increased toward the equilibrium Al concentration at each temperature in the late aging stage, compared with the initial Al concentration of c_p^{Al} = 0.2200.

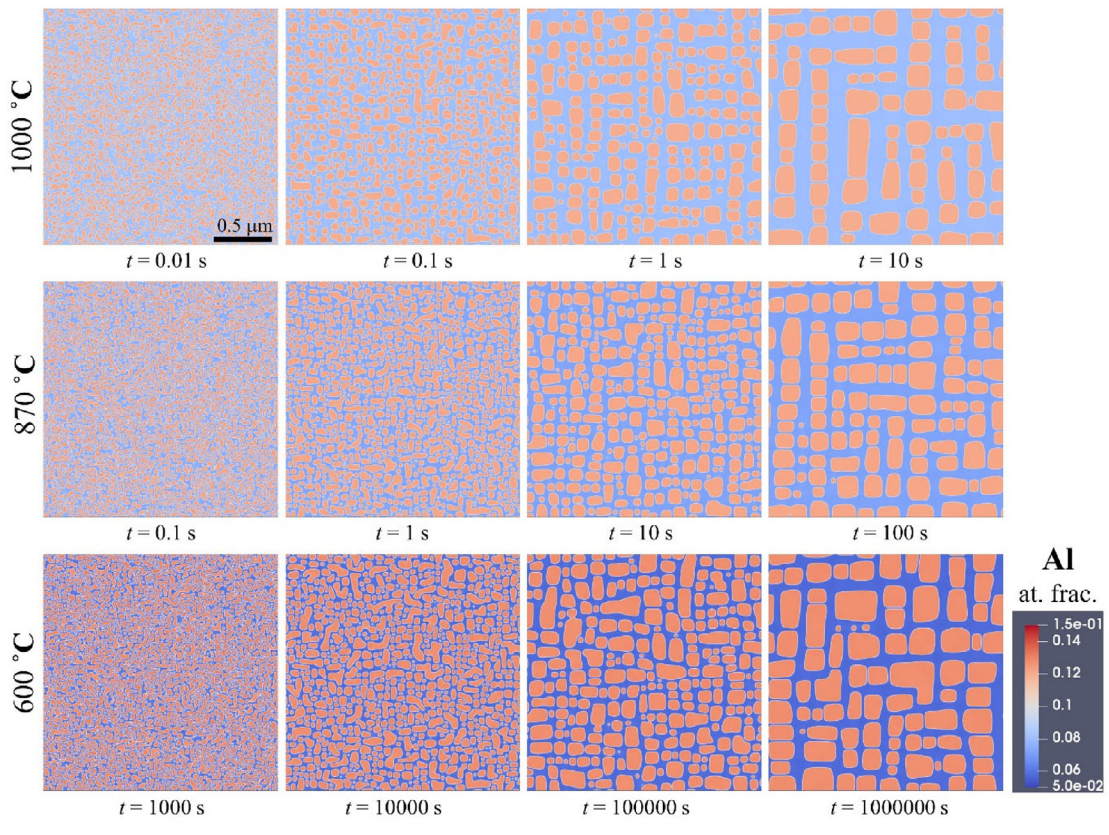

Fig. 4. Phase-field simulation results of microstructural evolution in Ni-Al binary alloy (Ni-19.11 at. % Al).

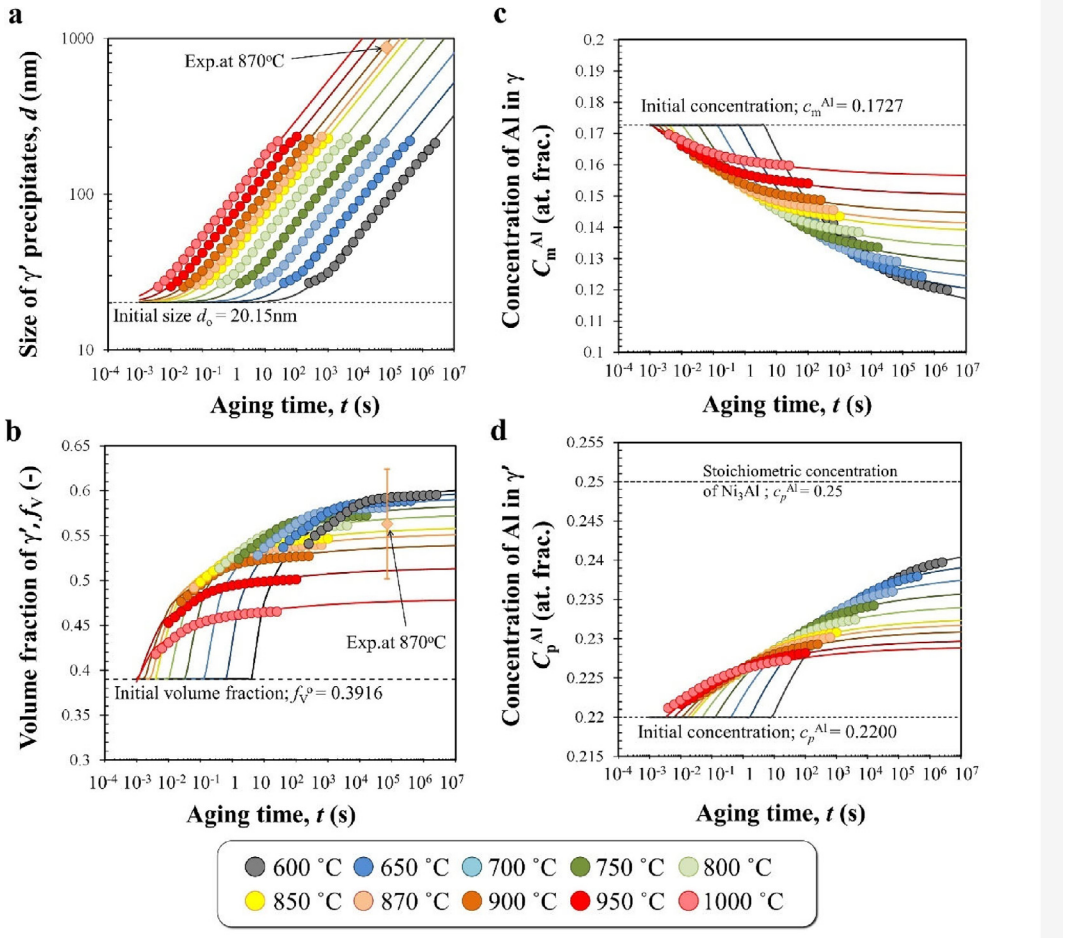

Fig. 5. Output results of phase-field simulation and image analysis module: (a) size of γ′, (b) volume fraction of γ′, (c) concentration of Al in γ, and (d) concentration of Al in γ′ during aging heat-treatment in Ni-Al binary alloy (Ni-19.11 at. % Al).

4.2. High-temperature strength

The output values from the PF simulation and image analysis modules can be passed to the strength prediction module to predict the 0.2 % proof stress of the alloy at any given test temperature. Fig. 6a shows a comparison of the 0.2 % proof stress experimentally obtained for various model alloys and the predicted 0.2 % proof stress via the mechanical property prediction module. The 0.2 % proof stress of the Ni-19.11 at. % Al model alloy with γ-γ′ two-phase structure (Fig. 3c) exhibited a clear inverse temperature dependence owing to the Ni_3Al with $L1_2$ structure exhibiting a significant inverse temperature dependence [39].

As mentioned in Section 2.4, the 0.2 % proof stress of the Ni-19.11 at. % Al alloy can be explained by a superposition of SSS, ROM strengthening, and precipitation strengthening. The 0.2 % proof stress predicted by inputting f_V = 56.3 %, d = 875 nm, and equilibrium Al concentration in γ at 870 °C, c_m^0 = 0.1405 was in good agreement with experimental values. Moreover, the 0.2 % proof stress of the Ni-10.27 at. % Al model alloy with γ single-phase structure decreased slightly with increasing test temperature. Additionally, the value was higher than that of pure Ni, thus implying clear SSS by 10.27 at. % Al addition. Furthermore, the predicted values *via* the SSS model, as mentioned in Section 2.4, were in good agreement with the experimental results. Therefore, the mechanical property prediction module was found to be useful for predicting the high-temperature strength of Ni-Al binary alloys.

Fig. 6b shows the time dependence of the predicted 0.2 % proof stress tested at 650 °C for the Ni-19.11 at. % Al alloy aged at 870 °C. Furthermore, the figure shows the contributions of solid-solution, ROM, and precipitation/dislocation interaction. The predicted 0.2 % proof stress gradually increased to the peak value t_p = 6.309 × 10^{-1} s and then gradually decreased with time. Evidently, this strength model adequately represents the over aging phenomenon of typical precipitation strengthened alloys. Here, the appearance of the peak value can be primarily explained by the strongly-coupled pair dislocation model (Fig. 2b). Note that the peak value appeared slightly later than the transition time t^* = 5.792 × 10^{-2} s for the weekly-coupled and strongly-coupled pair dislocation models (equation **(18)**). Moreover, the contribution of SSS (equation **(14)**) slightly decreased during this period owing to a gradual decrease in c_m^{Al} (Fig. 5**c**). In addition, the module represents that the contribution of ROM strengthening (equation **(17)**) gradually increases as f_V increases (Fig. 5b).

Furthermore, as shown in Fig. 6**c**, the peak value increased as the aging temperature decreased owing to the significant increase in f_V with decreasing temperature. The time t_p of the peak value became longer as the aging temperature decreased owing to the significant decrease in Al diffusion rate and the accompanying γ′ growth rate with a decrease in aging temperature. Note that the lines in Fig. 6b and 6c denote 0.2 % proof stress estimated by inputting microstructural features, such as f_V, d, c_m^{Al}, and c_p^{Al}, which are

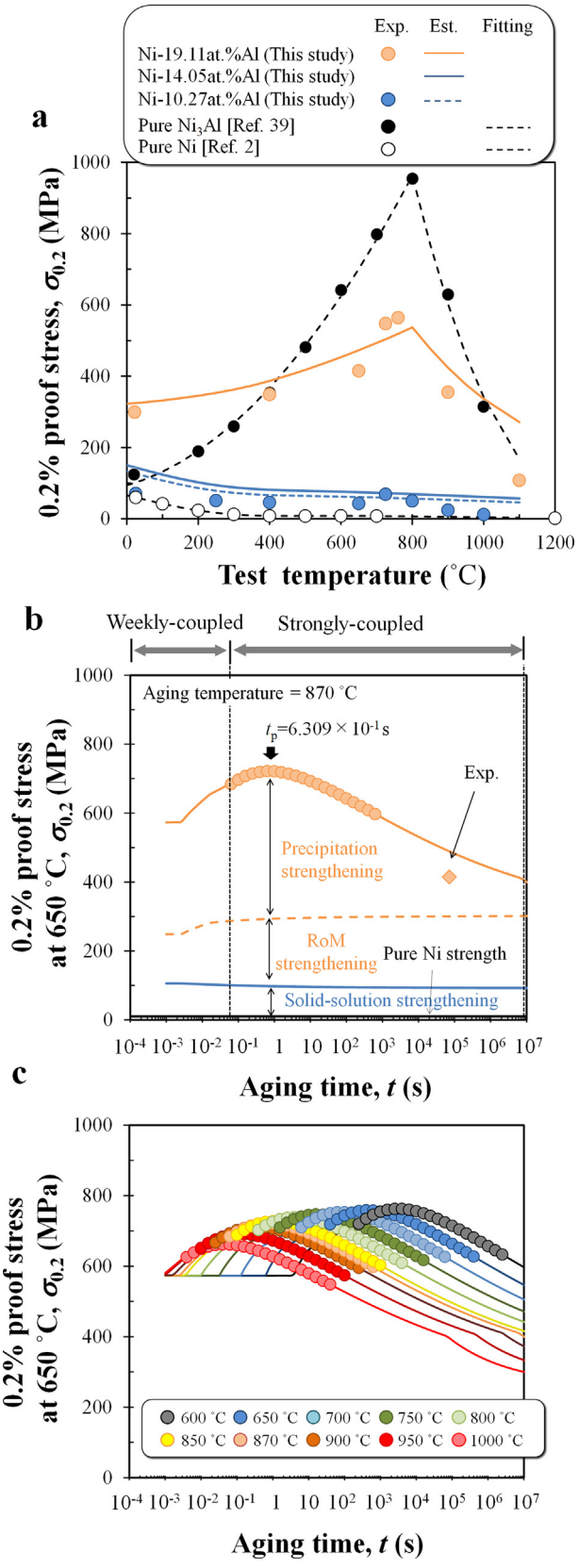

Fig. 6. Output results of mechanical property module: (a) modelling of temperature dependence of 0.2 % proof stress, (b) influence of aging time on 0.2 % proof stress at 650 °C, and (c) 0.2 % proof stress at 650 °C for several aging temperatures.

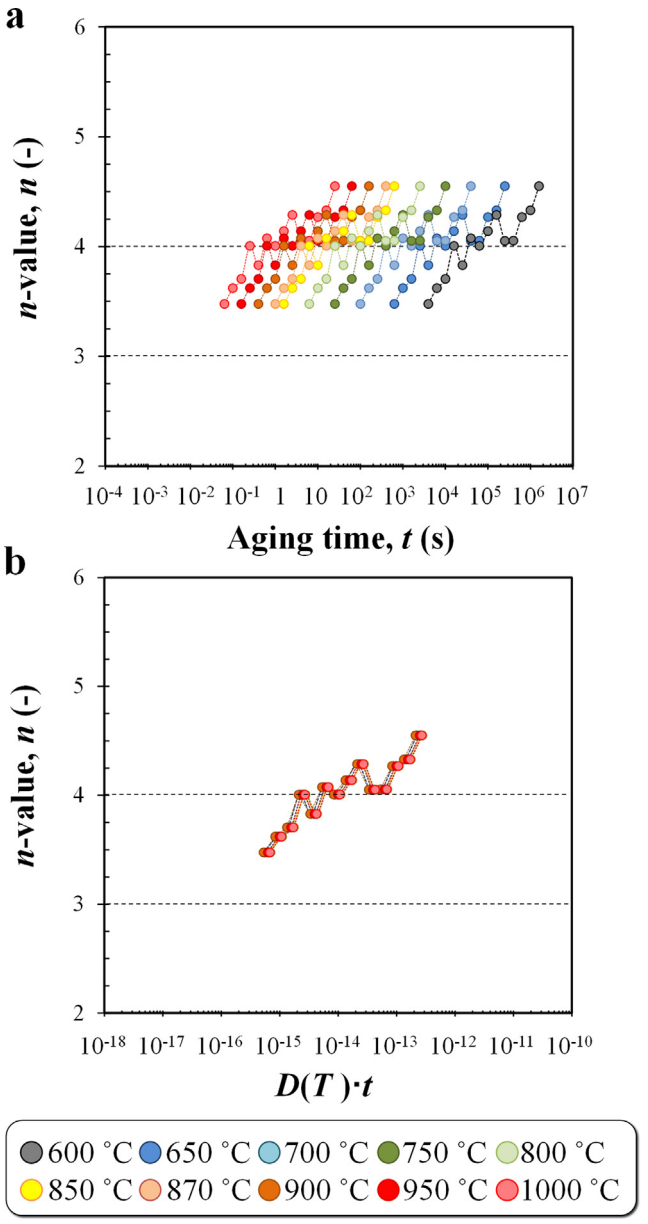

Fig. 7. (a) Temperature dependence on n value and (b) n value normalized using $D(T)\cdot t$.

calculated from equations (23), (28), (29), and (30), respectively (discussed in Section 5.2).

5. Discussion

The present workflow, which integrates the PF simulation, image analysis, and mechanical property prediction modules, provides an in-depth understanding of the effects of aging temperature, aging time, precipitate size d, volume fraction f_V and Al concentration c_m^{Al} in γ on the 0.2 % proof stress at elevated temperatures. In addition, the results obtained from the computer experiments are useful as virtual test results because obtaining a large amount of composition-structure–property data sets, including γ and γ′ compositions, would require a large amount of time and

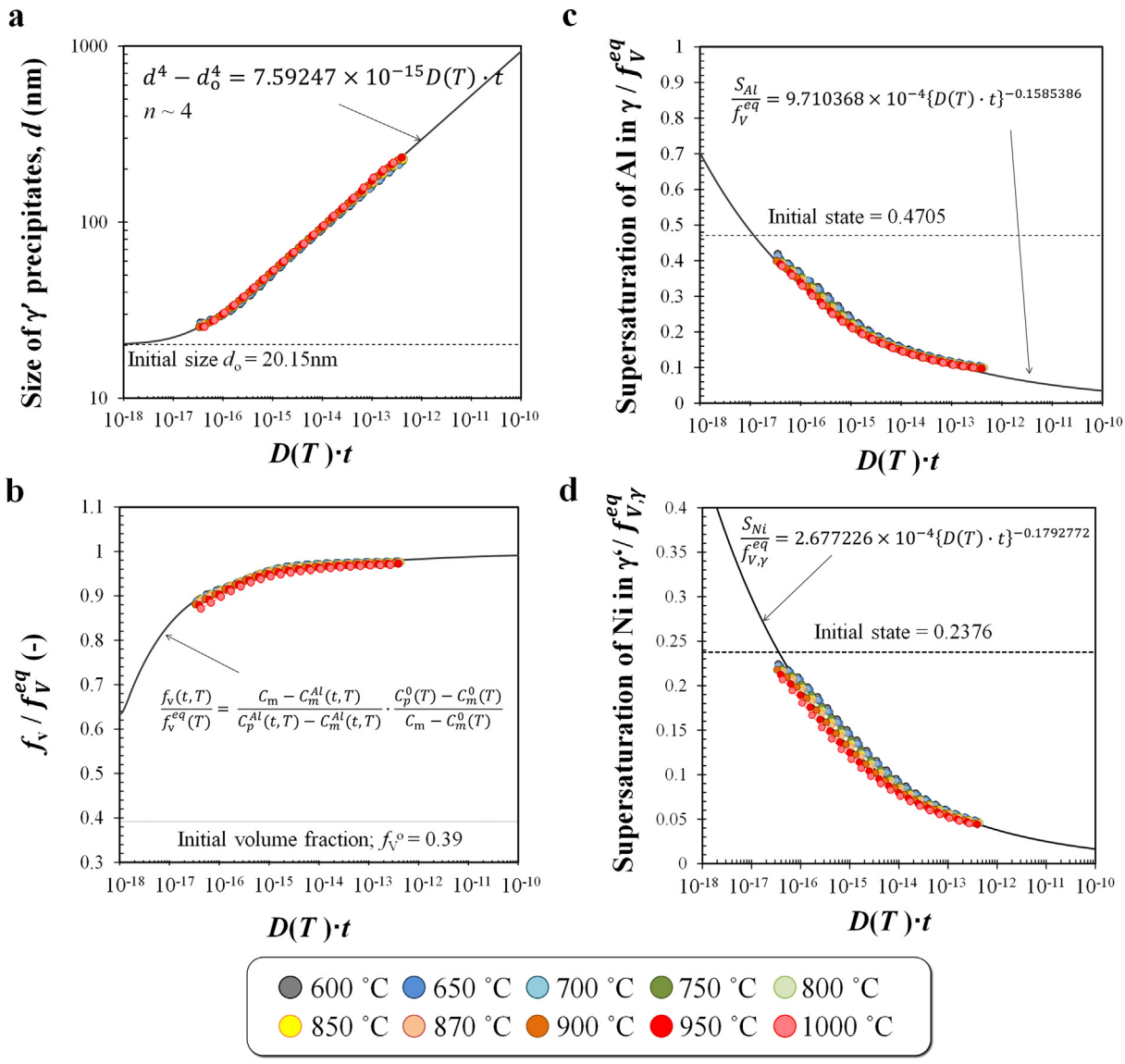

Fig. 8. Output results of phase-field simulation and image analysis module normalized using $D(T)\cdot t$; (a) size of γ′, (b) volume fraction of γ′, (c) concentration of Al in γ, and (d) concentration of Al in γ′ during aging heat-treatment in Ni-Al binary alloy (Ni-19.11 at. % Al).

effort in actual experiments. Here, the estimated composition-structure–property data sets with classical theories of microstructure evolution were compared and discussed.

5.1. Analysis of n-values for Ostwald ripening

The Lifshitz–Slyozov–Wagner (LSW) theory [46,47] is commonly known as a precipitation coarsening theory and is expressed in general form as:

$$d^n - d_o^n = Kt, \tag{20}$$

where K is the coarsening rate constant and is expressed in the LSW theory as:

$$K = \frac{64\sigma V_m^2 C_e}{9RT} D(T) = \frac{64\sigma V_m^2 C_e}{9RT} D_o \exp\left(\frac{-E_A}{RT}\right), \tag{21}$$

where σ is the interfacial energy density; V_m is the molar volume of second phase particles; C_e is the solvus limit of solute atoms, equivalent to c_{m^o}; R is the gas constant; and T is the aging temperature. In this study, D_o = 5.0 × 10^{-4} m^2s^{-1} and E_A = 2.60 × 10^5 $Jmol^{-1}{\cdot}K^{-1}$ were used (see Table 1). The n value is known to be 2 in the early stage of growth controlled by the interfacial reaction [48] and 3 in the later stage controlled by diffusion [49].

Furthermore, we assumed that K is constant at a constant temperature and only the time variation of the exponent n was considered. To discuss the time dependence of $n(t)$ at each aging temperature T from the d estimated in this study, the coarsening rate equation was defined as $d_i^{n(t_i)} - d_o^{n(t_i)} = Kt_i$ at discrete time t_i ($i \geq 1$) in the numerical calculation, and the following relationship was established at the small-time interval between t_i and t_{i+1}.

$$\frac{d_i^{n(t_{i+1})} - d_o^{n(t_{i+1})}}{d_i^{n(t_i)} - d_o^{n(t_i)}} = \frac{Kt_{i+1}}{Kt_i} = \frac{t_{i+1}}{t_i}, \tag{22}$$

where K was assumed constant (constant temperature). The value of $n(t_i) \cong n(t_{i+1})$ in the small-interval (t_i to t_{i+1}) and values of $n(t_i)$ in each interval can be calculated from equation (22).

Fig. 7a shows the relationship between the n-values obtained at T and t. Although the n value contains some errors owing to the finite discretization of time, the n value generally increased from 3.5 to 4.5. In the Ostwald ripening theory, the n value is known

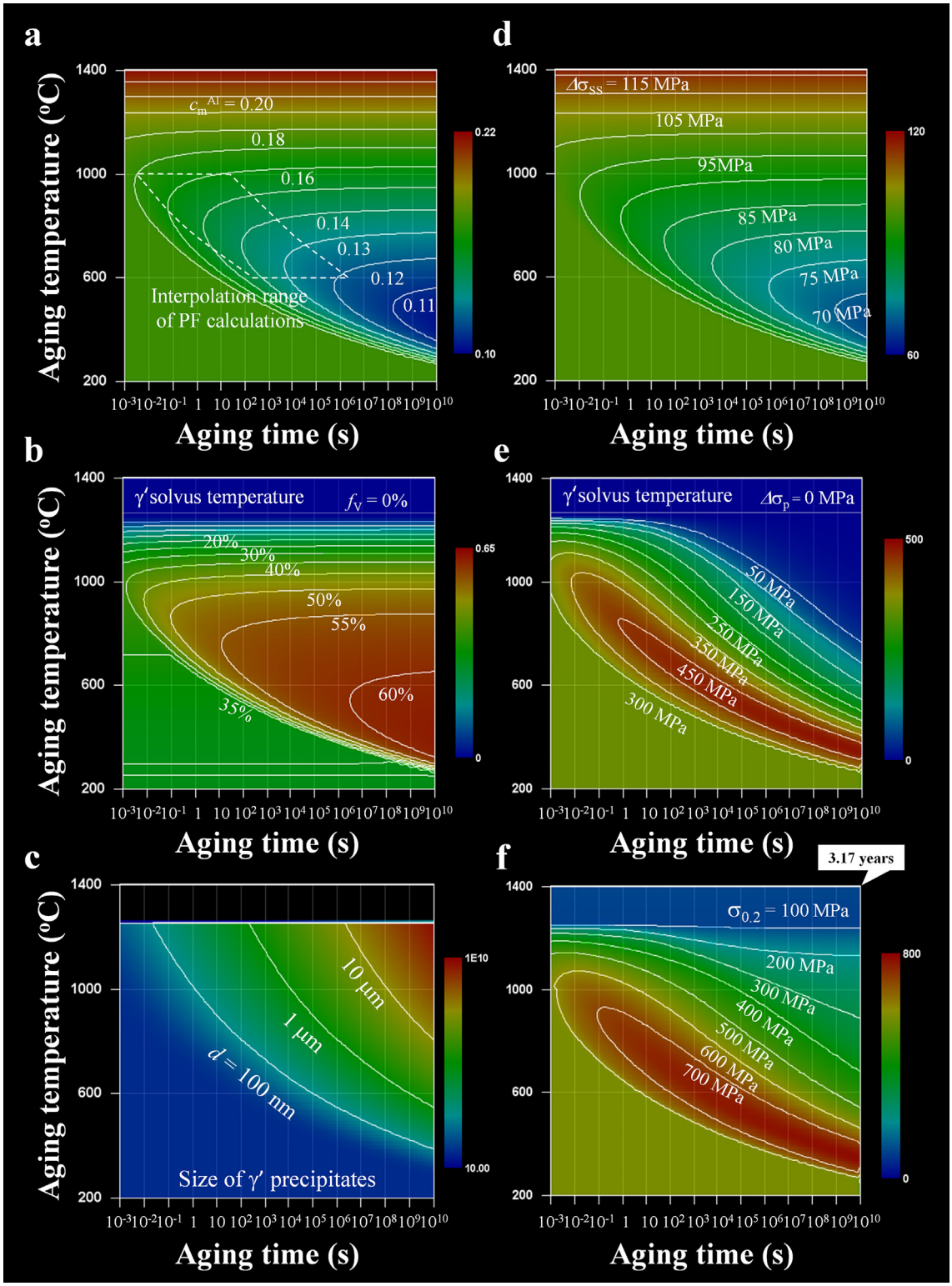

Fig. 9. Contour map showing dependence of aging temperature and time on (a) concentration of Al in g, (b) volume fraction of γ′, (c) size of γ′, strength increment by (d) solid solution strengthening, (e) precipitation strengthening, and (f) 0.2 % proof stress at 650 °C in Ni-Al binary alloy (Ni-19.11 at. % Al).

as 3. However, previous studies have experimentally demonstrated that the n value becomes higher when elastic interactions act between precipitates, resulting in a delay in coarsening [50,51].

As clearly shown in the microstructure in Fig. 4, the γ′ microstructure in this calculation results from coarsening behavior under strongly elastically constrained conditions; thus, the n value is approximately 4. Further, Fig. 7 indicates that the present PF module accurately considers the coherent strain field of the γ′ precipitates.

5.2. Numerical analysis by using normalized time

In this study, σ and V_m were treated as temperature-independent constants in the coarsening rate constant K in equa-

tion (21). In the Ni-Al binary phase diagram (Fig. 3a), $\frac{C_e}{T}$ could be approximated to a constant in the temperature range covered in this study. Therefore, the coefficient of $D(T)$ in equation (21) could be approximated to a constant. This result indicates that the time dependence of various parameters on temperature can be scaled by summarizing the time t in equation (20) as $D(T) \cdot t$. As shown in Fig. 7**b**, variations in the n-value with temperature can be normalized by replacing the time on the horizontal axis of Fig. 7**a** with $D(T) \cdot t$.

Furthermore, the normalized results using $D(T) \cdot t$ are shown in Fig. 8**a** – **8d** for all output results shown in Fig. 5**a** – **5d**, respectively. Here, these figures show the relationship between $D(T) \cdot t$ and precipitate size d; the ratio of γ' volume fraction f_V to the equilibrium volume fraction f_V^{eq}; the ratio of the Al supersaturation in γ, S_{Al}, to the γ' equilibrium volume fraction f_V^{eq}; and the ratio of the Ni supersaturation in γ', S_{Ni}, to the γ equilibrium volume fraction $f_{V,\gamma}^{eq}$. Here, f_V, f_V^{eq}, $f_{V,\gamma}^{eq}$, S_{Al}, and S_{Ni} are expressed as follows from the phase diagram in Fig. 3**a**.

$$f_V(t,T) = \frac{c_m - c_m^{Al}(t,T)}{c_p^{Al}(t,T) - c_m^{Al}(t,T)}, \tag{23}$$

$$f_V^{eq} = \frac{c_m - c_m^0(T)}{c_p^0(T) - c_m^0(T)}, \tag{24}$$

$$f_{V,\gamma}^{eq} = \frac{c_p^0(T) - c_m}{c_p^0(T) - c_m^0(T)}, \tag{25}$$

$$S_{Al}(t,T) = \frac{c_m^{Al}(t,T) - c_m^0(T)}{c_p^0(T) - c_m^0(T)}, \tag{26}$$

$$S_{Ni}(t,T) = \frac{c_p^0(T) - c_p^{Al}(t,T)}{c_p^0(T) - c_m^0(T)} \tag{27}$$

Note that all plots can be organized as a single curve in Fig. 8a – 8d.

Furthermore, as shown in Fig. 8a, the time dependence on d for each aging condition can be approximated using the following equation by setting n = 4, which is the average value in Fig. 7b. Evidently, the results are almost consistent with the calculation results.

$$d^4 - d_o^4 = 7.59247 \times 10^{-15} D(T) \cdot t \tag{28}$$

Additionally, the values estimated at each aging temperature from equation (28) are shown again in Fig. 5a. This illustrates that equation (28) can be confirmed to reproduce the precipitate size in Fig. 5a with high accuracy.

In Fig. 8c and 8d, the curve regressions of the obtained calculation results exhibit the following relationships.

$$\frac{S_{Al}}{f_V^{eq}} = \frac{c_m^{Al}(t,T) - c_m^0(T)}{c_m - c_m^0(T)} = 9.710368 \times 10^{-4} \{D(T) \cdot t\}^{-0.1585386}, \tag{29}$$

$$\frac{S_{Ni}}{f_{V,\gamma}^{eq}} = \frac{c_p^0(T) - c_p^{Al}(t,T)}{c_p^0(T) - c_m} = 2.677226 \times 10^{-4} \{D(T) \cdot t\}^{-0.1792772}, \tag{30}$$

where $c_m^0(T)$ and $c_p^0(T)$ were determined from the phase diagram summarized in Table 1; c_m= 0.1911 for Ni-19.11 at. % Al; and c_m^{Al} and c_p^{Al} at arbitrary aging temperature and time for this alloy can be estimated using equations (29) and (30), respectively. Here, the R^2-values for fitted lines, as shown in equations (29) and (30), were 0.9868 and 0.9816, respectively. Furthermore, as shown in Fig. 8b, $f_V(t,T)$ at arbitrary aging temperature and time could be estimated by substituting the estimated c_m^{Al} and c_p^{Al} into equation (23). Again, f_V, c_m^{Al}, and c_p^{Al} values estimated at each aging temperature from equations (23), (29), and (30) are shown in Fig. 5b – 5d, respectively. Evidently, the data analysis could reproduce the f_V, c_m^{Al}, and c_p^{Al} in Fig. 5b – 5d with high accuracy.

5.3. Composition-process-microstructure-strength mapping

As described above, d, f_V, c_m^{Al}, and c_p^{Al} at arbitrary aging temperature and time can be easily calculated by the numerical analysis formula of the PF simulation results using classical coarsening theory. Furthermore, by inputting these results into the model equation in Section 2.4, $\Delta\sigma_{ss}$, $\Delta\sigma_{\gamma'}^p$, and $\sigma_{0.2}$ can be estimated at an arbitrary aging temperature and time.

Fig. 9a – 9f show the contour plots of c_m^{Al}, f_V, d, $\Delta\sigma_{ss}$, $\Delta\sigma_{\gamma'}^p$, and $\sigma_{0.2}$ at 15,851 calculation points in the range of aging temperature (200–1400 °C) and aging time [ranging from 10^{-3} s to 10^{10} s (3.17 years)], respectively. The numerical analysis of PF simulation results conducted over a limited range and number of conditions enabled the creation of a wide range of high-resolution contour maps.

As shown in Fig. 9a, c_m^{Al} decreased with decreasing temperature and time and exponentially increased when it reached the equilibrium value. As shown in Fig. 9b, f_v increased with decreasing temperature. Evidently, aging for more than $t = 10^{10}$ s was required. For example, to reach the equilibrium values of c_m^0 = 0.1115 and f_V^{eq} = 0.609 at 600 °C. By contrast, as shown in Fig. 9c, the precipitate size increased with increasing aging temperature and time. For example, at 400 °C, the precipitates grew only up to d = 126.1 nm even after heat treatment for $t = 10^{10}$ s.

Further, as shown in Fig. 9d, the SSS $\Delta\sigma_{ss}$ was estimated by the c_m^{Al} value; thus, its contour map had a similar shape as Fig. 9a. Given that only Al solid solution strengthening was acting on the alloy, the maximum value of $\Delta\sigma_{ss}$ was 116.6 MPa, which is smaller than $\Delta\sigma_{\gamma'}^p$. Moreover, the minimum value was 67.90 MPa, which appeared at 430 °C for 10^{10} s.

By contrast, precipitation enhancement $\Delta\sigma_{\gamma'}^p$ was estimated by f_V and d, resulting in a contour map with distinct peak values. The maximum value of $\Delta\sigma_{\gamma'}^p$ was 486.9 MPa, which appeared under the conditions of T = 340 °C and $t = 10^{10}$ s.

The contour map of $\sigma_{0.2}$, estimated by the superposition of these strengthening mechanisms, was similar to that of $\Delta\sigma_{\gamma'}^p$, implying that the $\sigma_{0.2}$ of the γ-γ' two-phase alloy had a more significant contribution from precipitation strengthening than SSS. The maximum value of $\sigma_{0.2}$ was 764.7 MPa, which appeared at T = 340 °C and $t = 10^{10}$ s, is similar to $\Delta\sigma_{\gamma'}^p$. However, such a long aging time is impractical. For example, if 10^5 s (27.77 h) is set as a realistic aging time, the workflow can estimate that isothermal aging at 520 °C can realize the optimum combination of microstructural features (f_V = 58.42 %, d = 41.69 nm, and c_m^{Al} = 12.70 at. %), resulting in the maximum proof stress value of 769.0 MPa at 650 °C.

6. Conclusions

In this study, we focused on aging heat treatment, an important process that ultimately determines the properties of Ni-based alloys with a γ-γ' two-phase structure. Additionally, we established the computational workflow to predict mechanical properties from the heat treatment scheduling through the microstructure evaluation in Ni-Al binary alloys, which are a model example of Ni-based alloys. The workflow implemented in MInt was constructed by integrating the PF simulation, image analysis, and mechanical property prediction modules. The analysis of the

data computed with the workflow provides an in-depth understanding of the effects of aging temperature, aging time, precipitate size d, volume fraction f_V, and Al concentration c_m^{Al} in γ on the 0.2 % proof stress at elevated temperatures. Furthermore, the implementation of numerical analysis formulae on computer experiment results using classical coarsening theory easily realized the estimation of d, fv, c_m^{Al}, and c_p^{Al} over a wide range of aging temperatures and times. Therefore, the optimal aging process conditions and combination of multiple microstructural features that maximize mechanical properties can be discussed.

The most important feature of MInt is that it enables flexible and seamless integration with various modules. The present workflow provides a virtual test method for the aging process, which is a critical step in determining the high-temperature strength of this class of materials. Thus, placing the workflow after the modules may be helpful for forming processes modules, such as casting, forging, and 3D additive manufacturing [52]. In addition, with this workflow, a wide range of alloy systems can be accommodated by implementing commercially available or user-created thermodynamic equilibrium phase diagram information. In the future, this workflow can be expected to connect with various types of machine learning algorithms, such as Monte Carlo tree search, to automatically search for the optimal cost/performance solution in terms of heat treatment scheduling and composition [53,54].

Data availability

Data will be made available on request.

Declaration of Competing Interest

The authors declare that they have no known competing financial interests or personal relationships that could have appeared to influence the work reported in this paper.

Acknowledgements

This work was supported by the Council for Science, Technology, and Innovation (CSTI), Cross-ministerial Strategic Innovation Promotion Program (SIP), "Materials Integration for revolutionary design system of structural materials" (Funding agency: JST). We would also like to thank Mr. Takuma Kohata and Mr. Yuji Takata for extending their support in sample preparation and microstructural observation, and Mr. Yusuke Manaka for assisting with the implementation of the workflow on MInt. We would like to thank Editage (www.editage.com) for English language editing.

References

[1] H. Harada, H. Murakami, Design of Ni-base superalloys, in: T. Saito (Ed.), Computational Materials Design, Springer-Verlag, Berlin, 1999, pp. 39–70, https://doi.org/10.1007/978-3-662-03923-6_2.
[2] R.C. Reed, The Superalloys: Fundamentals and Applications, Cambridge University Press, New York, 2006. https://doi.org/10.1017/CBO9780511541285.
[3] T. Osada, Y. Gu, N. Nagashima, Y. Yuan, T. Yokokawa, H. Harada, Optimum microstructure combination for maximizing tensile strength in a polycrystalline superalloy with a two-phase structure, Acta Mater. 61 (2013) 1820–1829, https://doi.org/10.1016/j.actamat.2012.12.004.
[4] H.K.D.H. Bhadeshia, Computational design of advanced steels, Scr. Mater. 70 (2014) 12–17, https://doi.org/10.1016/j.scriptamat.2013.06.005.
[5] Y. Koizumi, T. Kobayashi, T. Yokokawa, Z. Jianxin, M. Osawa, H. Harada, Y. Aoki, M. Arai. Development of Next-Generation Ni-Base Single Crystal Superalloys. In: Superalloys 2004 (10th International Symposium). Vol 67. TMS; 2004: 35-43. https://doi:10.7449/2004/Superalloys_2004_35_43.
[6] R.C. Reed, T. Tao, N. Warnken, Alloys-by-design: application to nickel-based single crystal superalloys, Acta Mater. 57 (2009) 5898–5913, https://doi.org/10.1016/j.actamat.2009.08.018.
[7] W. Xiong, G.B. Olson, Cybermaterials: materials by design and accelerated insertion of materials, NPJ Comput. Mater. 2 (2016), https://doi.org/10.1038/npjcompumats.2015.9.
[8] E.I. Galindo-Nava, L.D. Connor, C.M.F. Rae, On the prediction of the yield stress of unimodal and multimodal γ' Nickel-base superalloys, Acta Mater. 98 (2015) 377–390, https://doi.org/10.1016/j.actamat.2015.07.048.
[9] N. Saunders, Z.-L. Guo, A.P. Miodownik, J.-P. Schillé, Modelling high temperature mechanical properties and microstructure evolution in Ni-based superalloys, Sente. Softw. Intern. Rep. 9 (2008). http://www.sentesoftware.co.uk/downloads/articles-and-papers.aspx%0Ahttps://drive.google.com/open?id=0B0fTxDBXtHZMTzF0Vl8xSjFZQmM.
[10] T.M. Pollock, H. Harada, T.E. Howson, J.J. Schirra, S. Walston, Superalloys 2016, Superalloys 2016 (2016) 849–858, https://doi.org/10.1002/9781119075646.
[11] M. Demura, Materials integration for accelerating research and development of structural materials, Mater. Trans. 62 (2021) 1669–1672, https://doi.org/10.2320/matertrans.MT-M2021135.
[12] M. Demura, T. Koseki, SIP-materials integration projects, Mater. Trans. 61 (2020) 2041–2046, https://doi.org/10.2320/matertrans.MT-MA2020003.
[13] T. Koyama, M. Ohno, A. Yamanaka, T. Kasuya, S. Tsukamoto, Development of microstructure simulation system in sip-materials integration projects, Mater. Trans. 61 (2020) 2047–2051, https://doi.org/10.2320/matertrans.MT-MA2020001.
[14] M. Enoki, Development of performance prediction system on SIP-MI project+1, Mater. Trans. 61 (2020) 2052–2057, https://doi.org/10.2320/matertrans.MT-MA2020007.
[15] J. Inoue, M. Okada, H. Nagao, H. Yokota, Y. Adachi, Development of data-driven system in materials integration+1, Mater Trans. 61 (2020) 2058–2066, https://doi.org/10.2320/matertrans.MT-MA2020006.
[16] S. Minamoto, T. Kadohira, K. Ito, M. Watanabe, Development of the materials integration system for materials design and manufacturing, Mater Trans. 61 (2020) 2067–2071, https://doi.org/10.2320/matertrans.MT-MA2020002.
[17] T. Osada, N. Nagashima, Y. Gu, Y. Yuan, T. Yokokawa, H. Harada, Factors contributing to the strength of a polycrystalline nickel-cobalt base superalloy, Scr. Mater. 64 (2011) 892–895, https://doi.org/10.1016/j.scriptamat.2011.01.027.
[18] L. Wu, T. Osada, T. Yokokawa, Y. Chang, K. Kawagishi, The temperature dependence of strengthening mechanisms in Ni-based superalloys: A newly re-defined cuboidal model and its implications for strength design, J. Alloys. Compd. 931 (2023), https://doi.org/10.1016/j.jallcom.2022.167508 167508.
[19] S.B. Biner, Programming phase-field modeling, Springer Cham, 2017. https://doi.org/10.1007/978-3-319-41196-5.
[20] N. Provatas, K. Elder, Phase-field methods in materials science and engineering, Wiley-VCH Verlag GmbH & Co. KGaA, 2010. https://doi.org/10.1002/9783527631520.
[21] I. Steinbach, Phase-field models in materials science, Model Simul. Mater. Sci. Eng. 17 (2009), https://doi.org/10.1088/0965-0393/17/7/073001 073001.
[22] Y. Wang, D. Banerjee, C.C. Su, A.G. Khachaturyan, Field kinetic model and computer simulation of precipitation of L12 ordered intermettalics from F.C.C. solid solution, Acta Mater. 46 (1998) 2983–3001, https://doi.org/10.1016/S1359-6454(98)00015-9.
[23] V. Vaithyanathan, L.Q. Chen, Coarsening of Ordered Intermetallic Precipitates with Coherency Stress, Vol 50, 2002. https://doi.org/10.1016/S1359-6454(02)00204-5.
[24] A.G. Khachaturyan, Theory of Structural Transformations in Solids, Dover Publications, 2013.
[25] S.G. Kim, W.T. Kim, T. Suzuki, Phase-field model for binary alloys, Phys. Rev. E – Stat. Physics, Plasmas, Fluids, Relat. Interdiscip. Top. 60 (1999) 7186–7197, https://doi.org/10.1103/PhysRevE.60.7186.
[26] N. Dupin, I. Ansara, B. Sundman, Thermodynamic re-assessment of the ternary system Al-Cr-Ni, Calphad Comput. Coupling Phase Diagrams Thermochem. 25 (2001) 279–298, https://doi.org/10.1016/S0364-5916(01)00049-9.
[27] T. Miyazaki, H. Imamura, T. Kozakai, The formation of "γ′ precipitate doublets" in NiAl alloys and their energetic stability, Mater. Sci. Eng. 54 (1982) 9–15, https://doi.org/10.1016/0025-5416(82)90024-6.
[28] The Japan Institute of Metals and Materials (Ed.), Metals Databook, 3rd ed, Maruzen Co., Ltd., 1993.
[29] Homepage of the visualization software. ParaView. https://www.paraview.org/,
[30] R.L. Fleischer, Substitutional solution hardening, Acta Metall. 11 (1963) 203–209, https://doi.org/10.1016/0001-6160(63)90213-X.
[31] R. Labusch, A statistical theory of solid solution hardening, Phys. Status. Solidi. 41 (1970) 659–669, https://doi.org/10.1002/pssb.19700410221.
[32] L.A. Gypen, A. Deruyttere, Multi-component solid solution hardening - Part 1 proposed model, J. Mater. Sci. 12 (1977) 1028–1033, https://doi.org/10.1007/BF00540987.
[33] M.X. Wang, H. Zhu, G.J. Yang, K. Liu, J.F. Li, L.T. Kong, Solid-solution strengthening effects in binary Ni-based alloys evaluated by high-throughput calculations, Mater. Des. 198 (2021), https://doi.org/10.1016/j.matdes.2020.109359 109359.
[34] I. Toda-Caraballo, P.E.J. Rivera-Díaz-Del-Castillo, Modelling solid solution hardening in high entropy alloys, Acta Mater. 85 (2015) 14–23, https://doi.org/10.1016/j.actamat.2014.11.014.
[35] B. Reppich, Materials Science and Technology Plastic Deformation and Fracture, sixth ed., R.W. Cahn, P. Haasen, R.T. Kramer (eds.), Wiley-VCH, 1993.
[36] Y. Mishima, S. Ochiai, N. Hamao, M. Yodogawa, T. Suzuki, Solid solution hardening of nickel—role of transition metal and B-subgroup solutes, Trans. Japan Inst. Met. 27 (1986) 656–664, https://doi.org/10.2320/matertrans1960.27.656.

[37] U.F. Kocks, Kinetics of solution hardening, Metall. Trans. A. 16 (1985) 2109–2129, https://doi.org/10.1007/BF02670415.
[38] O. Bouaziz, P. Buessler, Iso-work increment assumption for heterogeneous material behavior modelling, Adv. Eng. Mater. 6 (2004) 79–83, https://doi.org/10.1002/adem.200300524.
[39] M. Demura, D. Golberg, T. Hirano, An athermal deformation model of the yield stress anomaly in Ni_3Al, Intermetallics. 15 (2007) 1322–1331, https://doi.org/10.1016/j.intermet.2007.04.007.
[40] T. Kruml, B. Viguier, J. Bonneville, J.L. Martin, Temperature dependence of dislocation microstructure in Ni_3(Al, Hf), Mater. Sci. Eng. A. 234–236 (1997) 755–757, https://doi.org/10.1016/s0921-5093(97)00391-2.
[41] O.I. Gorbatov, I.L. Lomaev, Y.N. Gornostyrev, A.V. Ruban, D. Furrer, V. Venkatesh, D.L. Novikov, S.F. Burlatsky, Effect of composition on antiphase boundary energy in Ni3Al based alloys: Ab initio calculations, Phys. Rev. B. 93 (2016) 1–8, https://doi.org/10.1103/PhysRevB.93.224106.
[42] E. Chen, A. Tamm, T. Wang, M.E. Epler, M. Asta, T. Frolov, Modeling antiphase boundary energies of Ni3Al-based alloys using automated density functional theory and machine learning, NPJ Comput. Mater. 8 (2022) 1–10, https://doi.org/10.1038/s41524-022-00755-1.
[43] T. Murakumo, T. Kobayashi, Y. Koizumi, H. Harada, Creep behaviour of Ni-base single-crystal superalloys with various γ′ volume fraction, Acta Mater. 52 (2004) 3737–3744, https://doi.org/10.1016/j.actamat.2004.04.028.
[44] A. Miura, T. Osada, K. Kawagishi, K.I. Uchida, Thermal transport properties of Ni-Co-based superalloy, AIP Adv. 10 (2020), https://doi.org/10.1063/5.0030847.
[45] T. Miyazaki, H. Imamura, H. Mori, T. Kozakal, Theoretical and experimental investigations on elastic interactions between γ′-precipitates in a Ni-Al alloy, J. Mater. Sci. 16 (1981) 1197–1203, https://doi.org/10.1007/BF01033832.
[46] I.M. Lifshitz, V, V. Slyozov,, The kinetics of precipitation from supersaturated solid solutions, J. Phys. Chem. Solids. 19 (1961) 35–50, https://doi.org/10.1016/0022-3697(61)90054-3.
[47] C. Wagner, Theorie der Alterung von Niederschlägen durch Umlösen (Ostwald-Reifung), Z Elektrochem. 65 (1961) 581, https://doi.org/10.1002/bbpc.19610650704.
[48] P.R. Rios, T.G. Dalpian, V.S. Brandão, J.A. Castro, A.C.L. Oliveira, Comparison of analytical grain size distributions with three-dimensional computer simulations and experimental data, Scr. Mater. 54 (2006) 1633–1637, https://doi.org/10.1016/j.scriptamat.2006.01.007.
[49] S.D. Coughlan, M.A. Fortes, Self similar size distributions in particle coarsening, Scr. Metall. Mater. 28 (1993) 1471–1476, https://doi.org/10.1016/0956-716X(93)90577-F.
[50] T. Miyazaki, M. Doi, T. Kozakai, Shape bifurcations in the coarsening of precipitates in elastically constrained systems, Solid State Phenom. 3–4 (1991) 227–236, https://doi.org/10.4028/www.scientific.net/ssp.3-4.227.
[51] J.W. Martin, R.D. Doherty, B. Cantor, Stability of Microstructure in Metallic Systems (Cambridge Solid State Science Series), Cambridge University Press, second ed., 1997. https://doi.org/10.1017/CBO9780511623134.
[52] H. Kitano, M. Kusano, M. Tsujii, A. Yumoto, M. Watanabe, Process parameter optimization framework for the selective laser melting of hastelloy x alloy considering defects and solidification crack occurrence, Crystals. 11 (2021), https://doi.org/10.3390/cryst11060578.
[53] C.B. Browne, E. Powley, D. Whitehouse, S.M. Lucas, P.I. Cowling, P. Rohlfshagen, S. Tavener, D. Perez, S. Samothrakis, S. Colton, A survey of Monte Carlo tree search methods, IEEE Trans. Comput. Intell. AI Games. 4 (2012) 1–43, https://doi.org/10.1109/TCIAIG.2012.2186810.
[54] M. Dieb T, Ju S, Yoshizoe K, Hou Z, Shiomi J, Tsuda K., MDTS: automatic complex materials design using Monte Carlo tree search, Sci. Technol. Adv. Mater. 18 (2017) 498–503, https://doi.org/10.1080/14686996.2017.1344083.